The final report of work
for the period: January 1, 2001 - December 31, 2001

for

NASA grant NAG5-6001, Supplement (OSURF No. 740507)

Satellite and Model Analysis of the Atmospheric Moisture Budget
in High Latitudes

Subtitle:
High resolution precipitation over Greenland studied from dynamic method

Principal Investigator: David H. Bromwich
Co-Principal Investigator: Qiu-shi Chen

December 10, 2002

1 Introduction

Observations of precipitation over Greenland are limited. Direct precipitation measurements for the whole ice sheet are impractical, and those in the coastal region have substantial uncertainty (Bromwich and Robasky 1993) but may be correctable with some effort (Yang et al. 1999). However, the analyzed wind, geopotential height and moisture fields are available for recent years, and the precipitation is retrievable from these fields by a dynamic method. Based on recent Greenland precipitation from dynamic studies (Bromwich et al. 1993; the National Centers for Environmental Prediction (NCEP)/ National Center for Atmospheric Research (NCAR) Reanalysis (Kalnay et al., 1996); Chen et al., 1997a; European Centre for Medium-Range Weather Forecasts (ECMWF) Reanalysis for 1979-1993 (ERA-15) (Gibson et al. 1997)), several deficiencies in the precipitation spatial distributions from these dynamic methods were evaluated by Bromwich et al. (1998). Figures 1a and 1b show the distribution of the mean annual Greenland precipitation for 1979-1993 computed by the ERA-15 and that for 1985-1999 retrieved recently by the ω-equation method (Chen et al. 1997a; Bromwich et al. 2001a), respectively. Figure 1b is computed based on ECMWF operational data from TOGA Archive II of NCAR.

The snow accumulation, M_s, is determined by

$$M_s = P - E - D_{sn} - D_{mw} \tag{1}$$

where P and E are the rates of precipitation and evaporation/sublimation, and D_{sn} and D_{mw} are the horizontal mass divergence due to blowing snow and melting water, respectively. The precipitation is the most important source of accumulation, and on the other hand, the snow accumulation can be used to deduce the precipitation over ice sheets because it is the only quantity in (1) that can be measured at the ice core sites at the present time. Figure 1c shows the mean annual precipitation distribution over Greenland based on the modern synthesis by B. Csathó et al. (2002, personal communication), who used corrected precipitation totals from the coastal weather stations in addition to 253 accumulation values on the Greenland ice sheet. Box and Steffen (2001) showed that evaporation/sublimation is significant towards the coastal slopes. Their estimated evaporation/ sublimation values were added to the ice-sheet accumulation by B. Csathó et al. to approximate precipitation more closely in Fig. 1c. Although there is a temporal discrepancy of precipitation between the long-term average in Fig. 1c and that of recent years in Figs. 1a and 1b, comparison of the modeled precipitation (in Figs. 1a and 1b) with the directly and indirectly observed one (in Fig. 1c) can still be used to check the accuracy of the modeled precipitation.

It is easily seen that the distribution of precipitation in both Figs. 1a and 1b is much smoother than that in Fig. 1c. If the latitude $68^{\circ} N$ is used to separate Greenland into its northern and southern portions, there are two relative large precipitation areas shown in Fig. 1c in the western part of the northern Greenland. One is centered near the point $(70^{\circ} N, 47^{\circ} W)$ with a contour value of $50 \, cm \, yr^{-1}$ and the other is centered near the point $(76^{\circ} N, 63^{\circ} W)$ along the north shore of Baffin Bay. Although a relatively large precipitation area located at the latitude $70^{\circ} N$ can be found in both Figs. 1a and 1b, their central locations are a couple of degrees of longitude west from the relatively large center (at the point $(70^{\circ} N, 47^{\circ} W)$) as shown in Fig. 1c. In both Figs. 1a and 1b, there is no correspondingly large precipitation center near the point $(76^{\circ} N, 63^{\circ} W)$ along the north shore of Baffin Bay. In the east coast of the northern Greenland, Fig. 1c has many mesoscale features, but both Figs. 1a and 1b lack them. For example, there are several large precipitation centers located inland in the coastal region between $68^{\circ} N$ and $78^{\circ} N$ and a slight one is located $76^{\circ} N$ as shown in Fig. 1c, but these
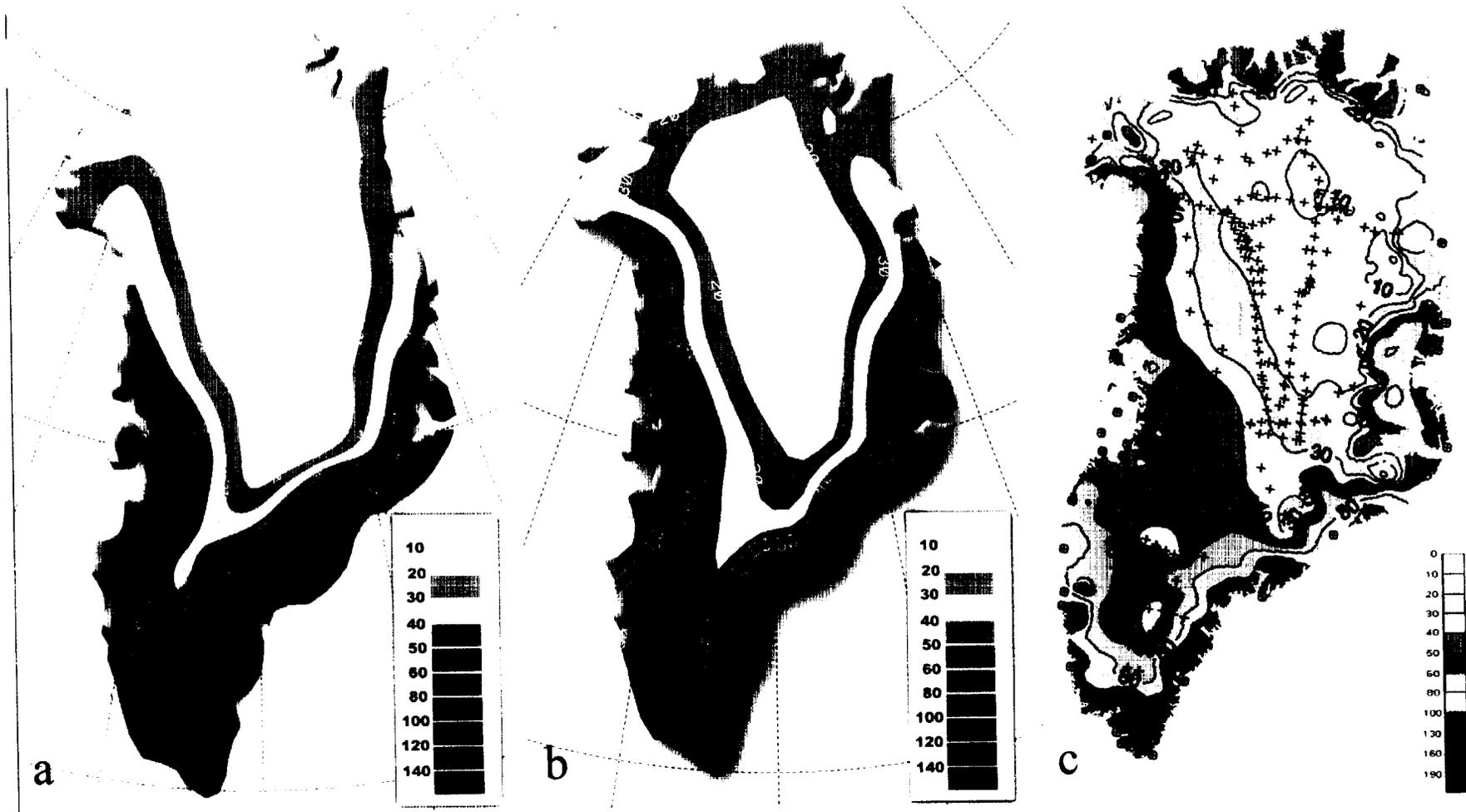
Fig.1. (a). The annual mean precipitation for 1979-1993 from ERA; (b). The annual mean precipitation for 1985-1999 retrieved by the improved ω-equation method (grid length: 50 km) (Bromwich et al, 2001a); (c) The annual mean precipitation distribution based on the modern synthesis by Csatho et al (2002, personal communication). (The map projection used in (c) is different from that used in (a) and (b).)

relatively large areas cannot be found in both Figs. 1a and 1b. In addition, there are also considerable differences in the western part of the southern Greenland between Fig. 1c and both Figs. 1a and 1b. The above comparisons show that the mesoscale features of the annual mean precipitation over Greenland in Figs. 1a and 1b need to be further improved.

The measured accumulation values from ice cores over Greenland have many unique features. The time scale of the measured accumulation is comparatively long. For example, only annual values can usually be obtained, thus the time scale of significant temporal variability is at least several years. For the annual time scale, the day-to-day variations are unimportant. However, the horizontal scale of the measured accumulation is very small. For example, the distance between some ice cores is a few kilometers, but the variations of the measured accumulation between them are often substantial. Thus, the horizontal scale of accumulation variations is only kilometers.

The mesoscale characteristics of the Greenland topography is the major factor causing the mesoscale features of the precipitation shown in Fig. 1c. During the computation of Fig. 1b, a high (50 km grid length) resolution Greenland topography has been used (Bromwich et al. 2001a), but the retrieved precipitation still fails to capture the mesoscale features. This is because the data sets (TOGA Archive from NCAR or ERA data) of the analyzed wind, geopotential height and moisture fields used in Figs. 1a and 1b must reflect the resolution of the topography adopted at the forecast center (here the ECMWF) from which the analyses originate; further the fields are sub-sampled to a resolution of $2.5^{o} \times 2.5^{o}$. These large scale resolution ($2.5^{o} \times 2.5^{o}$) data sets are inconsistent with the high resolution Greenland topography used in the computation of Fig. 1b. This inconsistency must have an important impact on producing the mesoscale features of the precipitation caused by the mesoscale topography.

Anthes (1990) showed that a mesoscale model with realistic treatment of mesoscale topography, earth surface conditions and physical processes is capable of developing mesoscale precipitation and phenomena from large-scale initial conditions. Physically, this means that a mesoscale model can produce mesoscale systems after a certain integration time through interactions and feedbacks between the large-scale initial conditions and the mesoscale topography, earth surface conditions and physical processes. In the interaction processes, the large scale initial wind and temperature fields evolve to be consistent with the mesoscale topography and physical processes and become the ones having mesoscale features.

The generalized ω-equation method studied by Chen et al. (1997a) is very useful for retrieving precipitation to study the mass balance over ice sheets. A reasonable precipitation description on the annual time scale with a relatively high horizontal resolution can be obtained by this method much more easily than by global and limited-area models. However, the generalized ω-equation is only a diagnostic relation; it derives precipitation immediately and does not include interactions and feedbacks between the large scale initial conditions and mesoscale topography even if the mesoscale topography is correctly specified. As shown in Fig. 1b, this method does not have the ability to generate enough mesoscale features of the Greenland precipitation from the large-scale initial conditions, which is an weakness of the ω-equation method in comparison to mesoscale models. In this paper, this diagnostic method is further developed and improved by using an iterative method to adjust the large-scale $2.5^{o} \times 2.5^{o}$ resolution analyzed data to be partially consistent with the high resolution Greenland topography. A balanced divergence equation is solved with the fixed external wind boundary condition (Chen et al. 1996) by iteration, and the new method is referred

to as the iterative balanced divergence equation method.

In a mesoscale model, the precipitation and atmospheric motion over mountainous regions, especially near steep slopes of mountains and ice sheets, are greatly influenced by the computational accuracy of the horizontal pressure gradient force over these regions. Colle et al. (1999) evaluated the 36- and 12-km resolution Penn State/NCAR mesoscale model (MM5) (Grell et al. 1994) precipitation forecasts and NCEP's 10-km resolution Eta Model (Eta-10) forecasts across the Pacific Northwest of the U.S. and found that the 12-km MM5 tends to generate too much precipitation along the steep windward slopes. The Eta-10 overpredicts precipitation along the windward slopes more than the 12-km MM5 even though the step-mountain approach of the Eta-coordinate system is used. The physical parameterizations of the MM5 have been adapted for applications over polar ice sheets (Bromwich et al. 2001b; Cassano et al. 2001) and the modified code is termed Polar MM5. Cassano et al. (2001) used the Polar MM5 to simulate a complete annual cycle from April 1997 through March 1998 over the Greenland Ice Sheet. The simulations are a series of 48-h forecasts of which only the forecasts of the second 24-h period are used to represent each day. The modeled precipitation distribution is excessive along the steep coastal margins with spot values in excess of 400 $cm\ yr^{-1}$ located on the southeast coast while the corresponding observed values are close to 120 $cm\ yr^{-1}$. The precipitation errors are similar to those over the Pacific Northwest found by Colle et al. (1999). Chen and Bromwich (1999) (hereafter referred to as CB99) showed that the horizontal pressure gradient force in sigma-coordinates can be computed more accurately by separating this horizontal vector into its irrotational and rotational parts, which are expressed by the equivalent geopotential and geo-streamfunction, respectively. This method has been successfully used by Chen et al. (1997a) and Bromwich et al. (1999; 2001a) in their ω-equation method to compute precipitation over the steep slopes of the Greenland ice sheet. Recently, this method has also been utilized in the MM5 to improve precipitation prediction over the steep slopes of mountains and ice sheets (Chen et al. 2001a,b).

In Section 2, the iterative balanced divergence equation method to adjust the large-scale $2.5'' \times 2.5''$ resolution analyzed data to be partially consistent with the high resolution Greenland topography is discussed, and a test of an annual precipitation over Greenland is shown by the method with and without iterations. In order to test the capability of this method for retrieval of the mesoscale features of the precipitation affected by topography over polar ice sheets, the annual mean precipitation distributions over Greenland from 1985-1999 computed by this method are shown in this section.

Because rises and falls of the ice surface elevation over a relatively short period are primarily produced by the snow accumulation, comparison of the interannual trend of precipitation with that of the observed surface elevation change over the Greenland ice sheet is discussed in Section 3.

2 An iterative balanced divergence equation method for improved retrieval of the meso-scale features of the annual precipitation over Greenland

a. The equivalent geopotential and geo-streamfunction in σ coordinates

The horizontal wind can be separated into its irrotational and rotational parts and expressed by

$$\vec{V} = -\nabla\chi - \vec{k} \times \nabla\psi$$

where χ and ψ denote velocity potential and streamfunction, respectively.

The vertical coordinate σ is defined by $\sigma = p/p_*$, where $p_*(x, y, t)$ is the surface pressure. The horizontal pressure gradient force (HPGF) $\vec{G}$ in σ-coordinates is expressed by

$$\vec{G} = -\nabla\phi(x, y, \sigma, t) - RT\nabla lnp_*(x, y, t) \tag{2}$$

where $\phi(x, y, \sigma, t)$ is the geopotential in σ coordinates. Here $\vec{G}$ is also a horizontal vector. *CB99* proposed that the vector G can also be separated into its irrotational and rotational components and expressed by

$$\vec{G} = -\nabla\phi_e - \vec{k} \times \nabla\eta \tag{3}$$

where $\phi_e(x, y, \sigma, t)$ and $\eta(x, y, \sigma, t)$ are referred to as an equivalent geopotential and a geo-streamfunction, respectively.

Because the divergence of the HPGF, $\nabla \cdot \vec{G}$, from the right hand side of (3) must be equal to that from the right hand side of (2), we have

$$\nabla^2\phi_e(x, y, \sigma, t) = \nabla^2\phi(x, y, \sigma, t) + \frac{\partial}{\partial x}\left(RT(x, y, \sigma, t)\frac{\partial lnp_*}{\partial x}\right) + \frac{\partial}{\partial y}\left(RT(x, y, \sigma, t)\frac{\partial lnp_*}{\partial y}\right) \tag{4}$$

In order to reduce computational errors in a limited region, a harmonic-sine spectral method (Chen and Kuo 1992) is used. Thus, the geopotential and equivalent geopotential in σ-coordinates can be separated into their inner and harmonic parts as

$$\phi = \phi_i(x, y, \sigma, t) + \phi_h(x, y, \sigma, t), \qquad \phi_e = \phi_{ei}(x, y, \sigma, t) + \phi_{eh}(x, y, \sigma, t) \tag{5}$$

where the inner part of the equivalent isobaric geopotential height in σ-coordinates, ϕ_{ei}, can be derived based on (4) from the solution of the following Poisson equation

$$\nabla^2\phi_{ei} = \nabla^2\phi_i + \frac{\partial}{\partial x}\left(RT\frac{\partial lnp_*}{\partial x}\right) + \frac{\partial}{\partial y}\left(RT\frac{\partial lnp_*}{\partial y}\right) \tag{6}$$

with zero Dirichlet boundary value.

Both $-\nabla\phi_e(x, y, \sigma, t)$ and $-\nabla\phi(x, y, p, t)$ are the irrotational part of the HPGF but they are in σ- and p-coordinates, respectively. Thus, the equivalent geopotential $\phi_e(x, y, \sigma, t)$ can be used in σ-coordinates in the same way as $\phi(x, y, p, t)$ is used in p-coordinates. The divergent and rotational parts of the HPGF are expressed by $\nabla^2\phi_e$ and $\nabla^2\eta$, respectively, and the divergence of the Coriolis force is denoted by $f_0\Omega$, where $f = f_0 + f'$, where f_0 is the average value of the Coriolis parameter in the integration region, and f' is its deviation from f_0. Here Ω is vorticity denoted as (2.1) of CB99. The divergence of the HPGF can be separated into its geostrophic and ageostrophic parts, where the geostrophic part is equal to $f_0\Omega$ as

$$\nabla^2\phi_{e,g} = f_0\Omega.$$

and the ageostrophic part of $\nabla^2\phi_e$ is the difference between $\nabla^2\phi_e$ and its geostrophic part and denoted by

$$\nabla^2\phi_{e,a} = \nabla^2\phi_e - f_0\Omega \tag{7}$$

Thus the divergence of the HPGF is the sum of its geostrophic and ageostrophic parts as

$$\nabla^2\phi_e = \nabla^2\phi_{e,g} + \nabla^2\phi_{e,a}$$

In the quasi-geostrophic approximation, the ageostrophic part of the divergence of the HPGF, $\nabla^2\phi_{e,a}$, always vanishes, thus we have

$$\nabla^2\phi_e = \nabla^2\phi_{e,g} = f_0\Omega = f_0\nabla^2\psi. \tag{8}$$

b. The vertical finite difference forms of the vorticity, divergence, continuity, hydrostatic and thermodynamic equations in σ coordinates

The vertical distribution of the variables is shown in Fig. 6 of CB99. In the present paper, 22 σ-levels at σ=0.010, 0.030, 0.050, 0.070, 0.090, 0.110, 0.140, 0.180, 0.220, 0.270, 0.340, 0.420, 0.505, 0.590, 0.670, 0.750, 0.820, 0.875, 0.920, 0.955, 0.980, and 0.995 are used in the vertical. Based on (5.9) and (5.10) of CB99, the vorticity and divergence equations are expressed by

$$\frac{\partial\Omega\downarrow}{\partial t} = -f_0 D\downarrow + \Omega_{adv}\downarrow \tag{9}$$

$$\frac{\partial D\downarrow}{\partial t} = f_0\Omega\downarrow -\nabla^2\phi_e\downarrow -\nabla^2 E\downarrow + D_{adv}\downarrow \tag{10}$$

where the column vector $X\downarrow$ of a variable X is denoted by

$$X\downarrow = (X_1, \quad ..., \quad X_k, \quad ..., \quad X_N)^T \tag{11}$$

and $(...)^T$ is for transpose, and N is the total number of σ-levels. Here the term $E_i\downarrow$ is denoted by $E_i\downarrow = [m^2(U^2 + V^2)_i/2]\downarrow$, and the terms $\Omega_{adv}\downarrow$ and $D_{adv}\downarrow$ are the variation rates of the vorticity and divergence caused by advection and denoted by (5.6) and (5.7) of CB99, respectively.

Based on (6.1) of CB99, the vertical finite difference form of the continuity equation is written as

$$\frac{\partial\ln p_*}{\partial t} + m_0^2\Pi D\downarrow_{\rightarrow} = P_{adv} \tag{12}$$

where $D\downarrow$ is the column vector of horizontal divergence and $\Pi_{\rightarrow}$ indicates the row vector as

$$\Pi_{\rightarrow} = (\Delta\sigma_1, \quad ..., \quad \Delta\sigma_k, \quad ..., \quad \Delta\sigma_N). \tag{13}$$

The map scale factor is separated by $m^2 = (m^2)_0 + (m^2)'$, and $(m^2)_0$ and $(m^2)'$ are the average value in the integration region and deviation, respectively. The term P_{adv} of (12) is dominated by the surface pressure advection and it is expressed by

$$P_{adv} = -m^2\sum_{j=1}^{N}\left(U_j\frac{\partial\ln p_*}{\partial x} + V_j\frac{\partial\ln p_*}{\partial y}\right)\Delta\sigma_j - (m^2)'\Pi D\downarrow_{\rightarrow} \tag{14}$$

The finite difference form of the hydrostatic equation based on (6.7) of CB99 is expressed by

$$\phi\downarrow = \phi_*\downarrow + R\mathbf{B}T\downarrow \tag{15}$$

where matrix $\mathbf{B}$ is a upper-triangular matrix shown by (A.29) of Chen et al. (1997b), and $\phi_*\downarrow = \phi_*\mathbf{I}$. Here $\mathbf{I}$ is the identity matrix and $\phi_* = gH_*$, where H_* is the height of the earth's surface.

The temperature can be separated into two parts

$$T(x,y,\sigma,t) = T_0(\sigma) + T'(x,y,\sigma,t) = T_0(\sigma) + (T(x,y,\sigma,t) - T_0(\sigma)) \tag{16}$$

where $T_0(\sigma)$ is the averaged value of $T(x, y, \sigma, t)$ over the constant $\sigma -$ surface, and T' is its deviation. The temperature separation (16) is different from that (5.2) and (6.9) of CB99 but is the same as that used by Chen et al. (1997b). The separation (16) is more natural than separation (5.2) and (6.9) used by CB99. Based on (2.28) of Chen et al. (1997b), the vertical difference form of the thermodynamic equation is written as

$$\frac{\partial T \downarrow}{\partial t} = T_{had} \downarrow -m_0^2 \mathbf{F} D \downarrow \tag{17}$$

where $\qquad T_{had} \downarrow = T_{adv} \downarrow -(m^2)' \mathbf{F} D \downarrow +P_T \downarrow$ $\qquad\qquad$ (18)

Here the matrix $\mathbf{F}$ is denoted by (A.34) of Chen et al. (1997b), and P_T is the diabatic heating.

c. The equations of the equivalent geopotential and ageostrophic part of the HPGF divergence

Substituting the inner part of the hydrostatic equation (15) into (6), the vertical difference form of (6) is expressed by

$$\nabla^2\phi_e \downarrow = \nabla^2\phi_* \downarrow +R\mathbf{B}\nabla^2 T \downarrow +\frac{\partial}{\partial x}\left(RT \downarrow \frac{\partial lnp_*}{\partial x}\right)+\frac{\partial}{\partial y}\left(RT \downarrow \frac{\partial lnp_*}{\partial y}\right) \tag{19}$$

Taking the partial derivative of (19) with respect to t, and utilizing (16), we have

$$\nabla^2\frac{\partial\phi_e \downarrow}{\partial t} = R\mathbf{B}\nabla^2\frac{\partial T \downarrow}{\partial t}+RT_0 \downarrow \nabla^2\frac{\partial \ln p_*}{\partial t}+\frac{\partial}{\partial x}\left(RT' \downarrow \frac{\partial}{\partial x}\frac{\partial \ln p_*}{\partial t}\right)+\frac{\partial}{\partial y}\left(RT' \downarrow \frac{\partial}{\partial y}\frac{\partial \ln p_*}{\partial t}\right)$$

$$+\frac{\partial}{\partial x}\left(R\frac{\partial T \downarrow}{\partial t}\frac{\partial \ln p_*}{\partial x}\right)+\frac{\partial}{\partial y}\left(R\frac{\partial T \downarrow}{\partial t}\frac{\partial \ln p_*}{\partial y}\right) \tag{20}$$

Comparing the above equation (20) with the similar equation (6.16) of CB99, there are additional two more last terms on the right hand side of (20). Substituting (12), (15), (16) and (17) into (20), then the equation of the HPGF divergence (20) becomes

$$\frac{\partial\nabla^2\phi_e \downarrow}{\partial t}+m_0^2\mathbf{A}D \downarrow = \nabla^2\Phi_{e,had} \downarrow \tag{21}$$

where matrix $\mathbf{A}$ is

$$\mathbf{A} = R\left(\mathbf{B}\mathbf{F}+T_0 \downarrow \underset{\rightarrow}{\Pi}\right) \tag{22}$$

and $\nabla^2\Phi_{e,had} \downarrow$ denotes the variation rate of the HPGF divergence caused by the advection and heating. For a variable X in a limited region, we have

$$X = X_i + X_h, \qquad (23), \qquad \nabla^2 X_h = 0. \tag{24}$$

Thus, $\nabla^2\Phi_{e,had} \downarrow$ can be rewritten as

$$\nabla^2\Phi_{e,had} \downarrow = \nabla^2\Phi_{e,had,i} \downarrow = R\mathbf{B}\nabla^2 T_{had,i} \downarrow +RT_0 \downarrow \nabla^2 P_{adv,i}$$

$$+R\left[T' \downarrow \nabla^2\left(P_{adv} - m_0^2\underset{\rightarrow}{\Pi}D \downarrow\right)_i +\frac{\partial T' \downarrow}{\partial x}\frac{\partial\left(P_{adv} - m_0^2\underset{\rightarrow}{\Pi}D \downarrow\right)}{\partial x}+\frac{\partial T' \downarrow}{\partial y}\frac{\partial\left(P_{adv} - m_0^2\underset{\rightarrow}{\Pi}D \downarrow\right)}{\partial y}\right]$$

$$+R\left[(T_{had} \downarrow -m_0^2\mathbf{F}D \downarrow)\nabla^2 lnp_{*i} +\frac{\partial(T_{had} \downarrow -m_0^2\mathbf{F}D \downarrow)}{\partial x}\frac{\partial lnp_*}{\partial x}+\frac{\partial(T_{had} \downarrow -m_0^2\mathbf{F}D \downarrow)}{\partial y}\frac{\partial lnp_*}{\partial y}\right] \tag{25}$$

There are two differences between the above equation (25) and similar equation (6.19) of CB99. One is that the variation rate of the HPGF divergence is used in (25) rather than that of the inner

part of the equivalent geopotential. The second is that there are two more additional terms on the right hand side of (25) than on that of (6.19) in CB99. With these two additional terms, the variation rate of the HPGF divergence caused by the advection and heating, $\nabla^2\Phi_{e,had}$ ↓, can be described more accurately.

Based on (7), the equation of the ageostrophic part of the HPGF divergence can be derived from (9) and (21) and expressed by

$$\frac{\partial\nabla^2\phi_{e,a}}{\partial t}\downarrow + m_0^2\mathbf{A}\nabla^2 D\downarrow -f_0^2 D\downarrow = \nabla^2\Phi_{e,had,a}\downarrow \tag{26}$$

where

$$\nabla^2\Phi_{e,had,a}\downarrow = \nabla^2\Phi_{e,had}\downarrow -f_0\Omega_{adv}\downarrow \tag{27}$$

is referred to as the variation rate of the ageostrophic part of the HPGF divergence caused by advection and diabatic heating.

d. The balanced divergence equation in σ-coordinates

If the tendencies of the divergence and ageostrophic part of the HPGF divergence in (10) and (26) are neglected, this approximation is referred to as a balanced ageostrophic approximation (Chen et al. 1996). In this case, equation (26) becomes

$$m_0^2\mathbf{A}\nabla^2 D_i\downarrow -f_0 D_i\downarrow = \nabla^2\Phi_{e,had,a}\downarrow . \tag{28}$$

Equation (28) is referred to as the balanced divergence equation in σ −coordinates, and it is also a divergence form of the generalized ω-equation. In this equation, the diabatic and advection terms computed by the ageostrophic wind are the same as those in the generalized ω−equation in p-coordinates (Pauley and Nieman 1992), but the effect of orography on the vertical motion is much better described than that in p-coordinates.

Equation (28) can be transformed into the equation of its vertical mode. We introduce a matrix **E** in order that the following relation is satisfied

$$\mathbf{E}^{-1}\mathbf{A}\mathbf{E} = \mathbf{G} = diag(gh_1, gh_2, ..., gh_N) \tag{29}$$

Let the velocity potential in the vertical mode and physical space are expressed by

$$D_{i*}\downarrow = \mathbf{E}^{-1}D_i\downarrow, \quad \text{and} \quad D_i\downarrow = \mathbf{E}D_{i*}\downarrow \tag{30}$$

respectively. Equation (28) is multiplied from left by the matrix $\mathbf{E}^{-1}$, and then its equation of the vertical mode separately is written as

$$C_k^2\nabla^2 D_{i*k} -f_0^2 D_{i*k} = \nabla^2\Phi_{e,had,a*k} +f_0^2 D_{h*k}, \qquad k = 1, \quad 2, ..., \quad N \tag{31}$$

where

$$\nabla^2\Phi_{e,had,a*}\downarrow = \mathbf{E}^{-1}\nabla^2\Phi_{e,had,a}\downarrow . \tag{32}$$

and

$$C_k = m_0\sqrt{gh_k} \tag{33}$$

Here C_k is the gravity-inertia wave phase speed for the k-th vertical mode, and

$$L_{0k}^2 = \frac{m_0^2 gh_k}{f_0^2} = \left(\frac{C_k}{f_0}\right)^2 \tag{34}$$

where L_{0k} is the radius of deformation of the k-th vertical mode.

From the solution D_i of (28), the divergence is computed by $D = D_i + D_h$. Using the continuity equation and vertical finite differencing, the pressure vertical velocity ω in σ coordinates is expressed by

$$\left(\frac{\omega}{p}\right)\downarrow = m^2(\mathbf{I}-\mathbf{C})\left(U\downarrow\frac{\partial \ln p_*}{\partial x}+V\downarrow\frac{\partial \ln p_*}{\partial y}\right)-m^2CD\downarrow \tag{35}$$

where $\mathbf{C}$ is a lower-triangular matrix and shown by (A.15) of Chen et al. (1997b).

The condensation method and the procedure for computing precipitation from the vertical motion are the same as those presented by Bromwich et al. (2001a).

e. An iterative solution of the balanced divergence equation with the fixed external wind boundary value

As pointed out in section 1, the ω-equation method cannot generate enough mesoscale features of the Greenland precipitation from the large-scale ($2.5'' \times 2.5''$) data sets even if the mesoscale topography is specified. This is because the large scale resolution data sets are generated from the same large scale topography and are not consistent with the high resolution topography. During the interpolation from the large scale ($2.5'' \times 2.5''$) data in p-coordinates to the high resolution ones in σ-coordinates, the surface pressure and temperature are computed based on the given high resolution topography and hydrostatic equation, and they are more consistent with the high resolution topography, especially the surface pressure. The horizontal wind is directly interpolated from the large scale p-coordinates to the new high resolution σ-coordinates, and it may not be consistent with the mass field (temperature and surface pressure) in σ-coordinates based on the high resolution topography. The balanced divergence equation (28) or (31) is one of the balanced equations used in the implicit nonlinear normal mode initialization (NNMI) (Temperton 1988) or balanced ageostrophic initialization (Chen et al. 1966) except that the equivalent geopotential and σ-coordinates are used here. The NNMI or balanced ageostrophic initialization is through an iterative method to adjust the unbalanced ageostrophic wind to be the balanced ageostrophic wind, and the initialized wind is the sum of the geostrophic and balanced ageostrophic winds (Chen et al. 1996). This basic result will not change if the equivalent geopotential and σ-coordinates are used. In the ω-equation method (Chen et al. 1997a; CB99), the vertical motion ω is computed from (35), in which only the divergence D is adjusted once through the solution of (31) but the wind components used in the advection term do not change. Thus, the vertical motion ω might be not adjusted enough and not consistent with the high resolution topography in this method. In the present section, the solution of the balanced divergence equation (31) is further adjusted by an iterative method as follows.

For the νth iteration, equation (31) can be written in the form

$$\left(\nabla^2 - \frac{1}{L_{0k}^2}\right)D_{i*k}^{(\nu)} = \frac{1}{C_k^2}\nabla^2\Phi_{e,had,a*k}^{(\nu-1)} + \frac{1}{L_{0k}^2}D_{h*k}^{(0)} \tag{36}$$

The harmonic part of the divergence $D_{h*k}^{(0)}$ in (36) is assumed to be unchanged in the iteration. The nonlinear term, $\nabla^2\Phi_{e,had,a*k}^{(\nu-1)}$ is calculated by using the values of $U^{(\nu-1)}\downarrow$, $V^{(\nu-1)}\downarrow$ and $D^{(\nu-1)}\downarrow$ at the $(\nu-1)$th step. At the beginning step, $\nu = 0$.

Equation (36) is solved easily by the double sine series due to their homogeneous boundary value for the inner parts, and its solution is directly expressed by

$$D_{i*k}^{(v)} = -F^{-1}\left[\left(\frac{1}{C_k^2}\nabla^2\Phi_{e,had,a*k,mn}^{(v-1)} + \frac{1}{L_{0k}^2}D_{h*k,mn}^{(0)}\right)\cdot\left(\frac{1}{L_{0k}^2}+\frac{1}{L_{mn}^2}\right)^{-1}\right] \tag{37}$$

where $F^{-1}[\cdots]$ is the inverse double sine Fourier transform operator denoted by (A.3) of CB99. During the above iteration, only the divergent component of the wind is modified within the region. Because the external wind is both nondivergent and irrotational in a limited region, no matter how the divergence is modified within the region, the external wind does not vary in the region and up to the boundary (Kuo and Chen 1992; Chen et al. 1996). Thus, it is very natural to use a fixed external wind as the lateral boundary condition in the iteration. If the interpolated wind components in a limited region bounded by Σ are given by the column vector as

$$U^{(0)}(x,y)\downarrow, \qquad V^{(0)}(x,y)\downarrow. \tag{38}$$

The external wind can be derived by the natural method (Chen et al. 1996) as follows. The vorticity, $\Omega^{(0)}\downarrow$, and divergence, $D^{(0)}\downarrow$, are computed from the wind components (39). The inner parts of the streamfunction and velocity potential are obtained by solving the Poisson equations

$$\nabla^2\psi_i^{(0)}\downarrow = \Omega^{(0)}\downarrow, \qquad \nabla^2\chi_i^{(0)}\downarrow = D^{(0)}\downarrow \tag{39}$$

with the homogeneous Dirichlet boundary values. The internal wind is computed by

$$U_I^{(0)}\downarrow = -\frac{\partial\psi_i^{(0)}\downarrow}{\partial y}+\frac{\partial\chi_i^{(0)}\downarrow}{\partial x}, \qquad V_I^{(0)}\downarrow = \frac{\partial\psi_i^{(0)}\downarrow}{\partial x}+\frac{\partial\chi_i^{(0)}\downarrow}{\partial y} \tag{40}$$

and the external wind is derived by

$$U_E^{(0)}\downarrow = U^{(0)}\downarrow - U_I^{(0)}\downarrow, \qquad V_E^{(0)}\downarrow = V^{(0)}\downarrow - V_I^{(0)}\downarrow. \tag{41}$$

In each iteration, it is necessary to compute the nonlinear advection terms, Ω_{adv} and $\nabla^2\phi_{e,adv}$ in (27). These nonlinear terms are computed by the transform method (Orszag 1970; Eliasen et al. 1970).

At v-th step, the inner part of the divergence $D_i^{(v)}$ is derived. The divergence is derived by

$$D^{(v)} = D_i^{(v)} + D_h^{(0)} \tag{42}$$

Thus, the inner part of the velocity potential can be derived from the Poisson equation

$$\nabla^2\chi_i^{(v)} = D^{(v)}. \tag{43}$$

with zero boundary value. The internal wind at v-th step is computed by

$$U_I^{(v)}\downarrow = \frac{\partial\chi_i^{(v)}\downarrow}{\partial x}-\frac{\partial\psi_i^{(0)}\downarrow}{\partial y} \qquad V_I^{(v)}\downarrow = \frac{\partial\chi_i^{(v)}\downarrow}{\partial y}+\frac{\partial\psi_i^{(0)}\downarrow}{\partial x} \tag{44}$$

The total wind is reconstructed by

$$U\downarrow^{(v)} = U_E^{(0)}\downarrow + U_I^{(v)}\downarrow, \qquad V^{(v)}\downarrow = V_E^{(0)}\downarrow + V_I^{(v)}\downarrow \tag{45}$$

where the external wind components, $U_E^{(0)}$ and $V_E^{(0)}$, are obtained from (41).

In the iteration, equation (35) can be expressed by

$$\left(\frac{\omega^{(v)}}{p}\right)\downarrow = m^2(\mathbf{I}-\mathbf{C})\left(U^{(v-1)}\downarrow\frac{\partial\ln p_*}{\partial x}+V^{(v-1)}\downarrow\frac{\partial\ln p_*}{\partial y}\right) - m^2\mathbf{C}D^{(v)}\downarrow \tag{46}$$

f. An example of the annual precipitation for 1986 over Greenland

Fig.2. (a). Topography of Greenland and adjacent areas (in m with a contour interval of 200 m based on the 25 km grid length): (b). The annual precipitation for 1986 retrieved by the method without iteration based on (48) with the 25 km grid length; (c). Same as (b) but computed by the iterative balanced divergence equation method based on (49).

In order to check how the mesoscale features of the computed precipitation is affected by the iteration, the annual precipitation for 1986 over Greenland is computed with and without iteration, respectively, but the other parameters are all the same. The computational domain and topography of Greenland are presented in Fig. 2a, and the modern terrain data set of Ekholm (1996) for Greenland topography is used. The mesh size is 111×71, and grid spacing is 25 km.

There are three methods which can be used to compute the pressure vertical velocity ω based on (35). The first method is to compute the pressure vertical velocity ω directly by

$$\left(\frac{\omega^{(0)}}{p} \right) \downarrow = m^2(\mathbf{I} - \mathbf{C}) \left(U^{(0)} \downarrow \frac{\partial \ln p_*}{\partial x} + V^{(0)} \downarrow \frac{\partial \ln p_*}{\partial y} \right) - m^2 \mathbf{C} D^{(0)} \downarrow \tag{47}$$

where $U^{(0)} \downarrow$ and $V^{(0)} \downarrow$ are interpolated from the $2.5'' \times 2.5''$ resolution data in p-coordinates to the 25 km resolution grid of the limited region in σ-coordinates, and the divergence $D^{(0)} \downarrow$ is computed from $U^{(0)} \downarrow$ and $V^{(0)} \downarrow$. The method (47) is referred to as a kinematic method. The horizontal divergence derived from this method is very sensitive to small errors of the interpolated wind components $U^{(0)} \downarrow$ and $V^{(0)} \downarrow$.

The second method is to derive pressure vertical velocity by

$$\left(\frac{\omega^{(1)}}{p} \right) \downarrow = m^2(\mathbf{I} - \mathbf{C}) \left(U^{(0)} \downarrow \frac{\partial \ln p_*}{\partial x} + V^{(0)} \downarrow \frac{\partial \ln p_*}{\partial y} \right) - m^2 \mathbf{C} D^{(1)} \downarrow \tag{48}$$

where the divergence $D^{(1)} \downarrow$ is derived from the divergence equation (28), in which the forcing term $\nabla^2 \Phi_{e,had,a*} \downarrow$ based on (27) has two terms of similar magnitude. Thus, the divergence $D^{(1)} \downarrow$ derived from (28) is much less sensitive to the wind errors than $D^{(0)} \downarrow$ computed from the kinematic method. The method (48) may be referred to as the ω-equation method without iteration, and it was used by Chen (1997a) and Bromwich et al. (1999, 2001a) except that $D^{(1)} \downarrow$ is derived from the velocity potential form of the equation (28). In this method, the vertical velocity $\omega^{(1)} \downarrow$ is more accurate and more consistent with the high resolution topography than $\omega^{(0)} \downarrow$.

In the third method, the divergence $D^{(1)} \downarrow$ is further used to improve divergent component of the wind by using (44) and (45) to obtain $U^{(1)} \downarrow$ and $V^{(1)} \downarrow$. Then $U^{(1)} \downarrow$ and $V^{(1)} \downarrow$ can be used to improve the horizontal advection in the forcing term of (35) to derive $D^{(2)} \downarrow$, and the vertical velocity $\omega^{(2)} \downarrow$ is computed by

$$\left(\frac{\omega^{(2)}}{p} \right) \downarrow = m^2(\mathbf{I} - \mathbf{C}) \left(U^{(1)} \downarrow \frac{\partial \ln p_*}{\partial x} + V^{(1)} \downarrow \frac{\partial \ln p_*}{\partial y} \right) - m^2 \mathbf{C} D^{(2)} \downarrow \tag{49}$$

The third method based on (49) is referred to as an iterative balanced divergence equation method. In general, this iterative method converges rapidly, and it is accurate enough to let the value of ν be 2 or 3. In the present paper, that $\nu = 2$ is used in the iterative method.

As an example, the distribution of the annual precipitation for 1986 over Greenland computed from (48) with the 25-km grid length without the iteration is shown in Fig. 2b. Comparing Fig. 2b with Fig. 1b, it is seen that, although the grid length used in Fig. 2b is a half of that used in Fig. 1b, the distribution of precipitation in Fig. 2b is quite similar to that in Fig. 1b and its mesoscale features are not improved. Figure 2c depicts the annual precipitation of the same year computed by the iterative balanced divergence equation method based on (49). Figure 2c has many mesoscale features of the precipitation, especially a relatively large area near the point $(70'' N, 47'' W)$ and a center near the point $(76'' N, 63'' W)$ along the north shore of Baffin Bay in the west coastal region of Greenland. In the east coast of the northern Greenland, there are two relatively large mesoscale precipitation

Fig.3. The mean annual precipitation over Greenland for 1985-1999 retrieved by the iterative balanced divergence equation method.

centers located inland in the coastal region between $68°N$ and $78°N$, and similar to Fig. 1c, the smaller one is located $76°N$ as shown in Fig. 2c. Thus, the precipitation in Fig. 1c is more similar to the annual precipitation in Fig. 2c than to that in Fig. 2b. This example shows that the iterative balanced divergence equation method has capability of improving the mesoscale features of precipitation over Greenland affected by the high resolution topography.

g. The retrieved mean annual precipitation distribution of the Greenland for 1985-1999

The mean annual precipitation distribution over Greenland computed by this method for 1985-99 is shown in Fig. 3, which is calculated based on the ECMWF operational data (TOGA Archive II from NCAR), the topography of Fig. 2a at 25 km resolution and the 22 levels in the vertical of the model.

Comparing Fig. 3 with Fig. 1b, it is seen that the distribution of the mean annual precipitation in Fig. 3 has much more mesoscale features than that in Fig. 1b. The two relatively large accumulation areas, which are centered near the point $(70°N, 47°W)$ and along the north shore of Baffin Bay at the point $(76°N, 63°W)$, respectively, in the western part of the northern Greenland shown in Fig. 1c, have been retrieved in Fig. 3, but they are not simulated well by the method without iteration as discussed in Section 1. The areas encircled by the contours of 10 and 20 $cm\ y^{-1}$ over the central Summit region depicted in Fig. 1c are more similar to those in Fig. 3 than in Fig. 1b. For example, the area around by the closed contour of 10 $cm\ y^{-1}$ in Fig. 1b is too large, which means that the modeled result in Fig. 1b is too dry over the central Summit region. This weakness has been improved in Fig. 3. In the east coast of the northern Greenland, there are two relatively large mesoscale precipitation centers located inland in the coastal region between $68°N$ and $78°N$ in Fig. 3: the strong one is located at $76°N$ while the weak one is located at $76°N$. These two mesoscale areas are similar to those in Fig. 1c, but they are not retrieved in Fig. 1b. In addition, the significant precipitation errors in the south of $65°N$ of the west coastal region of the southern Greenland in Fig. 1b (in comparison with Fig. 1c) have also been corrected in Fig. 3. The mesoscale distributions of both Figs. 3 and 1c in this region are quite similar. However, the differences of the mesoscale distributions along the west coast between $65°N$ and $72°N$ in Figs. 1c and 3 are different, and these mesoscale differences of the precipitation in this region need to be further studied. From all of the above comparisons, it is seen that many features of the annual mean precipitation over Greenland which could not be retrieved by the method without iteration as shown in Fig. 1b have been greatly improved in Fig. 3.

3 Comparison of the interannual trend of the precipitation with the observed surface elevation change for 1993-1999 over the Greenland ice sheet

a. The equation of variation of the ice sheet surface elevation

The variation rate of the surface elevation of an ice sheet, dH_{ice}/dt, is determined by

$$\frac{dH_{ice}}{dt} = M_s - D_f \tag{50}$$

where M_s, and D_f denote the variation rates of the surface elevation caused by accumulated snow and firn densification, respectively. Here M_s is expressed in snow depth rather than in water equivalent. The firn densification only changes the snow surface elevation but does not alter the

net water equivalence, and it may also be referred to as snow deflation. Based on (1), equation (50) can be rewritten for a relatively short time period as

$$\frac{dH_{ice}}{dt} = P - E - D_{sn} - D_{mw} - D_{f} \tag{51}$$

As D_s in (50), the terms P, E, D_{sn} and D_{mw} in (51) are all expressed in snow depth rather than in water equivalent. Because the precipitation is a very important source in accumulation, it is also very important for the change of the surface elevation of ice sheets. In order to understand what is responsible for the changes of the surface elevation of the Greenland ice sheet, it is necessary to study the corresponding precipitation changes.

b. The interannual trend for 1993-1999 of the Greenland precipitation at elevations above 2000 meters

Recent advances in airborne laser altimetry and global positioning system (GPS) technology have made possible the large-scale assessment of elevation change characteristics of the entire ice sheet through repeated surveys separated in time. Such repeated surveys in 1993 and 1998 (Krabill et al. 1999) showed that the southeast margin of the Greenland ice sheet has been thinning. Aircraft laser-altimeter surveys over northern Greenland in 1994 and 1999 have also been studied by Krabill et al. (2000), and they reported changes in the surface elevation of Greenland between 1993 and 1999 derived from radar and laser altimetry and estimated coastal melting. It is found that, above 2000 meters elevation, the entire ice sheet is in balance on average but has some regions of local thickening or thinning. The changes of surface elevation of the Greenland ice sheet above 2000 m are shown in Fig. 4a.

Above 2000 m surface elevation, most of the northern ice sheet lies above the region of summer melting. McConnell et al. (2000) derived changes of the ice-sheet elevation in southern Greenland for the years 1978-88, using a physically based model of firn densification and records of annual snow accumulation reconstructed from 12 ice cores at elevations above 2000 meters elevation. They found that the patterns of elevation change derived from snow accumulation agree closely with contemporaneous satellite measurements of the surface elevation change of the ice sheet. Thus, the effects of melting on the surface elevation change of southern Greenland above 2000 m should also be small.

In order to compare the temporal variability of precipitation with that of the surface elevation over Greenland above 2000 m, the spatial distribution of the slope of the linear regression line of the annual precipitation from the balanced divergence method for 1993-1999 has been computed. A color-coded figure of the slope of the linear regression line of the annual precipitation from 1993-1999 over Greenland above 2000 m is shown in Fig. 4b. It should be pointed out that the unit used in precipitation is cm/year in water equivalent, and a multiplying factor of about 3.3 is necessary to transform the water equivalent values to the thickness of snow (R. Thomas, personal communication, 2001) in Fig. 4b.

In southern Greenland (south of $70^{\circ} N$) above 2000 m, there are three thinning areas in both Figs. 4a and 4b. Two thinning regions are located to the south of $67^{\circ} N$ over its eastern part and western part, respectively. The strength and area of these thinning regions over the eastern part are larger than those over the western part. It should also be noted that the colors of contour spacing used in Figs. 4a and 4b are not the same. There are two other thinning regions centered in $69.5^{\circ} N, 47^{\circ} W$ and $69.5^{\circ} N, 34^{\circ} W$, respectively shown in both Figs. 4a and 4b. There are three
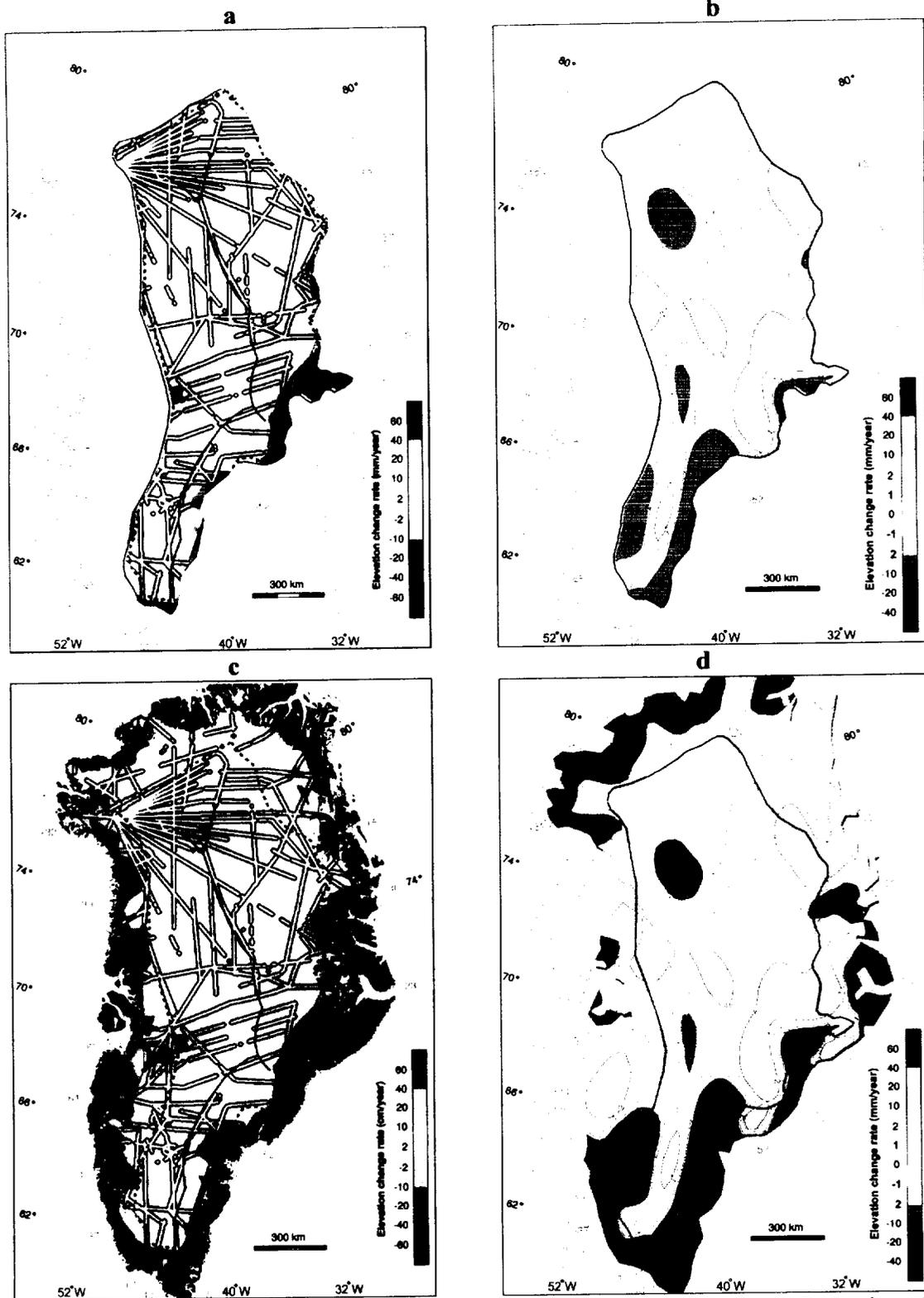
Figure 4 a) A part of Fig. 4c for Greenland ice-surface elevation change in the region above 2000 m; b) A part of Fig. 4d for annual precipitation trend in the region above 2000 m; c) Greenland ice-surface elevation change *dh/dt* in unit *cm/year* for 1993-1999 derived mostly from airborne laser-altimetry. The 13 coastal stations are shown in green along with the *dh/dt* value derived from the PDD anomalies (Krabill et al. 2000); d) the annual precipitation trend over Greenland computed by the iterative balanced divergence method in unit *cm/year*.

thickening areas located at about $(68°N, 37°W)$, $(65°N, 47°W)$ and $(62.5°N, 48°W)$ shown in both Figs. 4a and 4b. Thus, the central locations of thinning and thickening areas in the southern Greenland above 2000m in Figs. 4a and 4b are in good agreement with each other.

In northern Greenland (north of $70°N$) above 2000 m, there are two major thickening regions centered at about $(72°N, 48°W)$ and $(76°N, 28°W)$ and two weak thinning areas centered at about $(76°N, 44°W)$ and $(73°N, 29°W)$ shown in Fig. 4a. These two thickening and two thinning regions correspond to two positive and two negative areas of precipitation change respectively centered at about the same locations in Fig. 4b. One positive precipitation increase region centered at about $(71°N, 32°W)$ shown in Fig. 4b is not matched to a thickening area in Fig. 4a. This may be due to deficiencies in the interannual variation of the precipitation retrieval or other causes, for example, relatively large melting in this region.

From the above, it is seen that the Greenland ice sheet above 2000 meters elevation from 1993-1999 is nearly in balance with some regions of local thickening or thinning, and the altimetry-derived ice-sheet thickening and thinning are approximately consistent with the precipitation change. This situation was first discussed by Bromwich et al. (2001a). Because some mesoscale features of the precipitation over Greenland have been improved by the balanced divergence equation method, the newly computed annual precipitation trend is compared again with the observed changes of the ice sheet surface elevation, and the results are in better agreement with the measured local thinning and thickening.

c. The interannual precipitation trend for 1993-1999 at the elevation below 2000 meters of Greenland and the downward trend for 1993-1999 over southern Greenland

At elevations below 1700 m, radar altimeter data become unreliable (Thomas et al. 1999). Krabill et al. (2000) calculated a hypothetical thinning rate at the coast on the basis of the coast positive degree day (PDD) anomalies, using a factor of 9 mm per PDD. From their approach, only melt is considered near coast in the thinning rate. They excluded measured surface elevation change in coastal areas; instead, an interpolation was used between the calculated PDD thinning rates due to melting and nearest observed elevation changes to yield thinning rates over the ice-covered coastal regions. Based on their method, the annual trend of the surface elevation of the Greenland ice sheet including the region above 2000 m is shown in Fig. 4c. Below 2000 m surface elevation, Fig. 4c shows that thinning predominates at lower elevations along about 70% of the coastal regions, with rates about 1 meter per year close to the coast. The thinning rates exceeding 1 m/year over the coastal areas shown in Fig. 4c are probably too large to be caused by melting only.

Based on (51), changes of surface elevation over the ice sheet are due to not only the melting but also precipitation, evaporation/sublimation, firn densification and drifting snow. Thus, it is not appropriate that only melting is considered in estimating the change of surface elevation of ice sheet even in the coastal areas. In order to get a relatively accurate estimate of surface elevation change over the whole Greenland ice sheet, especially the region below 2000 m, not only precipitation but also the melting, evaporation/sublimation, firn densification and drifting snow need to be studied in the modeling and diagnostic studies.

The slope of the linear regression line of the annual precipitation from 1993-1999 over Greenland including the regions above and below 2000 m is shown in Fig. 4d. It is clear that the linear trends over the coastal region on the average is negative, especially with relatively large negative values in the coastal regions of southern Greenland. The linear trends in annual precipitation from

1985-1999 for Greenland have also been calculated, similar negative values are also found in the coastal regions of southern Greenland (figure omitted). Thus, there is a significant downward trend in annual precipitation from 1985-1999 for the southern Greenland and its coastal regions. This result is consistent with the report of Bromwich et al. (1999) that a significant downward trend in annual precipitation from 1985-1995 for all of Greenland and its southern and central-west coastal regions, amounting to 3% per year had been retrieved by the dynamic method (Chen et al. 1997a). The similar results for 1985-1999 were also shown by Bromwich et al. (2001a) based on the improved dynamic method.

4 Conclusion

Based on the studies shown in the above sections, the following conclusions can be reached.

(1) The advatage of the generalized ω-equation method in σ-coordinates developed by Chen et al. (1997a) and CB99 is to obtain a reasonable precipitation over steep slopes of the Greenland ice sheet in the annual time scale more easily than global and limited-area models, but its weakness is not able to generate the mesoscale features of the Greenland precipitation very well from the large-scale initial conditions. The generalized ω-equation method is further developed now by using an iterative method to adjust the large-scale $2.5^\circ \times 2.5^\circ$ resolution analyzed wind to be partially consistent with the high resolution topography. In this method the balanced divergence equation is solved by iterations with the fixed external wind lateral boundary condition, thus, this method is further referred to as the iterative balanced divergence method. The computed results show that this iterative method has good capability in computing the mesoscale features of the annual mean precipitation affected by high resolution topography from the large scale analyzed wind.

Many mesoscale features of the mean annual precipitation distribution over Greenland are retrieved by the iterative balanced divergence method. For example, the two relative large precipitation areas, which are centered near the point $(70^\circ N, 47^\circ W)$ and near the point $(76^\circ N, 63^\circ W)$ along the north shore of Baffin Bay in the western part of Greenland, are retrieved, but they are not simulated by the original ω-equation method without iteration. The computed mean precipitation over the central Summit region is also improved to be quite similar to the observed precipitation.

(2) The Greenland ice sheet above 2000 meters elevation from 1993-1999 is nearly in balance with some regions of local thickening or thinning, and the altimetry-derived ice-sheet thickening and thinning are approximately consistent with the precipitation change. Because some mesoscale features of the precipitation over Greenland have been improved by the balanced divergence equation method, the computed annual precipitation trend is in good agreement with the measured local thinning and thickening. In order to get a relatively accurate estimate of surface elevation change over the whole Greenland ice sheet, especially the region below 2000 m, not only precipitation but also the melting, evaporation/sublimation, firn densification and drifting snow need to be studied in the modeling and diagnostic studies.

The linear precipitation trend over the coastal region on the average is negative, especially with a relatively large negative value in the coastal regions of southern Greenland. There is a significant downward trend in annual precipitation from 1985-1999 for the southern Greenland and its coastal regions.

5 References

Anthes, R. A., 1990: Recent applications of the Penn State/NCAR mesoscale model to synoptic, mesoscale, and climate studies. *Bull. Amer. Meteor. Soc.*, **71**, 1610-1629.

Box, J. E., and K. Steffen, 2001: Sublimation estimates for the Greenland Ice Sheet using automated weather station observations. *J. Geophys. Res.*, **106**(D24), 33,965 - 33,982.

Bromwich D. H., F. M. Robasky, R. A. Keen, and J. F. Bolzan, 1993: Modeled variations of precipitation over the Greenland Ice Sheet. *J. Climate*, **6**, 1253-1268.

Bromwich D. H., and F. M. Robasky, 1993: Recent precipitation variations over the polar ice sheets. *Meteor. Atmos. Phys.*, **51**, 259-274.

Bromwich D. H., R. I. Cullather, Q.-S. Chen, and B. M. Csatho, 1998: Evaluation of recent precipitation studies for the Greenland ice sheet. *J. Geophys. Res.*, **130**(D20), 26,007-26,024.

Bromwich, D. H., Q.-S. Chen, Y. Li, and R. I. Cullather, 1999: Precipitation over Greenland and its relation to the North Atlantic Oscillation. *J. Geophys. Res.*, **104**(D18), 22,103 - 22,115.

Bromwich, D. H., Q.-S. Chen, L. Bai and Y. Li, 2001a: Modeled precipitation variability over the Greenland ice sheet. *J. Geophys. Res.*, **106**(D24), 33,891 - 33,908.

Bromwich, D. H., J. J. Cassano, T. Klein, G. Heinemann, K. M. Hines, K. Steffen, and J. E. Box, 2001b: Mesoscale modeling of katabatic winds over Greenland with the Polar MM5. *Mon. Wea. Rev.*, **129**, 2290-2309.

Cassano, J. J., J. E. Box, D. H. Bromwich, L. Li, and K. Steffen, 2001: Evaluation of Polar MM5 simulations of Greenland's atmospheric circulation. *J. Geophys. Res.*, **106**(D24), 33,867 - 33,890.

Chen, Q.-S., and Y.-H. Kuo, 1992: A harmonic-sine series expansion and its application to the partitioning and reconstruction problem in a limited area. *Mon. Wea. Rev.*, **120**, 91-112.

Chen, Q.-S., Y.-H. Kuo and D. H. Bromwich, 1996: A balanced ageostrophic initialization with a fixed external wind boundary value for limited-area models. *J. Meteor. Soc. Japan*, **74**, 325-342.

Chen, Q.-S., D. H. Bromwich and L. Bai, 1997a: Precipitation over Greenland retrieved by a dynamic method and its relation to cyclonic activity. *J. Climate*, **10**, 839-870.

Chen, Q.-S., L. Bai and D. H. Bromwich, 1997b: A harmonic-Fourier spectral limited-area model with an external wind lateral boundary condition. *Mon. Wea. Rev.*, **125**, 143-167.

Chen, Q.-S., and D. H. Bromwich, 1999: An equivalent isobaric geopotential height and its application to synoptic analysis and to a generalized ω-equation in σ-coordinates. *Mon. Wea. Rev.*, **127**, 145-172.

Chen, Q-S., D. H. Bromwich and L. Bai, 2001a: Greenland precipitation variability in recent years retrieved by an initialization dynamic method and its relation to atmospheric circulation, Preprint of Sixth Conference on Polar Meteorology and Oceanography, 14-18 May 2001, San Diego, CA. Amer. Meteor. Soc., 57-60.

Chen, Q-S., L. Bai and D. H. Bromwich, 2001b: Application of the equivalent geopotential to the Penn/NCAR mesoscale model (MM5) for improving precipitation prediction over mountainous regions, Preprint of Ninth Conference on Mesoscale Processes, 30 July - 2 August 2001, Fort Lauderdale, FL, Amer. Meteor. Soc., 151-154.

Colle B. A., K. J. Westrick, and C. F. Mass, 1999: Evaluation of MM5 and Eta-10 precipitation forecasts over the Pacific Northwest during the cool season. *Weather and Forecasting, 14,* 137-154.

Ekholm, S., 1996: A full coverage, high-resolution, topographic model of Greenland computed from a variety of digital elevation data. *J. Geophys. Res.,* **101**(B10), 21,961 - 21,972.

Eliasen, E., B. Machenauer and E. Rasmussen, 1970: On the numerical method for integration of the hydrodynamic equations with a spectral representation of the horizontal fields. *Inst. of Theor. Met. Univ. of Copenhagen, Report No. 2.* 35 pp.

Gibson J. K., P. Kallberg, S. Uppala, A. Hernandez, A. Nomura, and E. Serrano, 1997: ERA description. ECMWF Re-Analysis Project Report series 1, 72 pp. (Available from ECMWF Shinfield Park, Reading, RG2 9AX, United Kingdom).

Grell, G. A., J. Dudia, and D. R. Stauffer, 1994: A Description of the Fifth-Generation Penn State/NCAR Mesoscale Model (MM5), NCAR Tech. Note NCAR/TN-398+STR.

Kalnay, E., and 21 others, 1996: The NCEP/NCAR 40-year reanalysis project. *Bull. Amer. Meteor. Soc.,* **77**, 437-471.

Krabill, W., E. Frederick, S. Manizade, C. Martin, J. Sonntag, R. Swift, R. Thomas, W. Wright, and J. Yungel, 1999: Rapid thinning of parts of the southern Greenland ice sheet. *Science,* **283**, 1522-1524.

Krabill, W., W. Abdalati, E. Frederick, S. Manizade, C. Martin, J. Sonntag, R. Swift, R. Thomas, W. Wright, and J. Yungel, 2000: Greenland ice sheet: High-elevation balance and peripheral thinning, *Science,* **289**, 428-430.

McConnell, J. R., R. J. Arthern, E. Mosley-Thompson, C. N. Davis, R. C. Bales, R. Thomas, J. F. Burkhart, and J. F. Kyne, 2000: Changes in Greenland ice sheet elevation attributed primarily to snow accumulation variability. *Nature,* **406**, 877-879.

Orszag, S. A. 1970: Transform method for calculation of vector coupled sum: application to the spectral form of the vorticity equation. *J. Atmos. Sci.* **27**, 890-895

Pauley, P. M., and S. J. Nieman, 1992: A comparison of quasi-geostrophic and nonquasi-geostrophic vertical motions for a rapidly intensifying marine extratropical cyclone. *Mon. Weather Rev.,* **120**, 1108-1134.

Temperton, C., 1988: Implicit normal mode initialization. *Mon. Wea. Rev.,* **116**, 1013-1131.

Thomas, R., C. Davis, E. Frederick, S. Manizade, J. Sonntag, W. Krabill, and J. McConnell, 1999: Greenland ice sheet elevation change since 1978 from radar and laser altimetry. *Polar Geogra.,* **23**, 169-184.

Yang, D., S. Ishida, B. E. Goodison, and T. Gunther, 1999: Bias correction of daily precipitation measurements over Greenland. *J. Geophys. Res.,* **104**, 6171-6181.